Physics Student Works

Physics

12-2022

Supercontinuum Light Generation via Non-linear Effects in Hollow-Core Fiber

Skyler Gulati

Citation

Gulati, S. (2022). Supercontinuum Light Generation via Non-linear Effects in Hollow-Core Fiber. *Physics Student Works.* Retrieved from https://scholarworks.uark.edu/physstuwo/1

Supercontinuum Light Generation via Non-linear Effects in Hollow-Core Fiber

By Skyler Preet Gulati

Submitted to University of Arkansas Department of Physics

Fall 2022

Undergraduate Thesis Advised by Dr. Hiroyuki Nakamura

University of Arkansas

Table of Contents

Abstract

The field of non-linear optics has gained traction in the last couple decades due to the variable generation of wavelengths which are less deterministic than within traditional optics. Using non-linear mediums, including hollow-core fibers (HCF), generation of wavelengths spanning into the vacuum ultraviolet (VUV) wavelength range is possible. These short wavelengths can be utilized within electron spectroscopy-based methods of material science like angle-resolved photoemission spectroscopy (ARPES). This technique most often uses specific photoemission lines of atoms in discharge lamps, however, with the frequency dispersion capabilities of HCF, broad band creation can allow for variable wavelength selection through filtering specific wavelengths with the continuation of ultrashort pulses in the femtosecond time domain. These characteristics could enhance the field of photoemission spectroscopy. The production of such wavelengths is driven through multiple non-linear effects, including the Kerr effect, high harmonic generation, Raman effect, etc. Using a HCF of 100 mm and an 80 MHz pulsed laser source with a central wavelength of 745 nm, I was able to develop a supercontinuum spanning from <190 nm to >1000 nm.

Keywords: Hollow-Core Fiber, Supercontinuum, Non-Linear Optics, Undergraduate Research

Acknowledgments

I would like to thank Dr. Nakamura for the continued support, knowledge, and resources to begin my career within in Physics. I'm aware it is no easy goal to advise and jumpstart students within this field while also balancing your own career and am eternally grateful for this opportunity bestowed upon me.

I would like to recognize the assistance those within Dr. Nakamura's lab group have provided with the hours of helping me pursue my research but also help understand how to be successful within the field of non-linear optics.

Finally, I want to thank my family including my parents, Arun and Joanne Gulati, alongside my brothers, Justin and Devon Gulati, for keeping me motivated during the most stressful periods of my undergraduate education. You all provided the light I needed to continue my research within Optics.

Supporting Grants

The Undergraduate Research Grant provided through the Office of Undergraduate Research funded by the University of Arkansas. Vacuum-Ultraviolet Light Generation via Non-linear Effects in Hollow-Core Fiber for Photoelectron Spectroscopy. Awarded January 2022 in the amount of $3,250, supervised by Dr. Hiroyuki Nakamura.

Introduction and Motivation

Vacuum-ultraviolet light (VUV) is characterized as wavelengths ranging from 10 nm to 200 nm, this spectral range spans approximately from 6 eV to 120 eV. This wavelength range contains enough energy to overcome the work function of a variety of materials (to knock electrons out of a molecule or atom). For example, gold (Au)'s work function is 5.1 eV, so ionization can occur from wavelengths under 200 nm. This form of photoionization was only discovered in the 20th century. Angle-resolved photoemission spectroscopy [7] (ARPES) which utilizes this photoelectron effect [8] has become one of the most powerful techniques to investigate the electronic properties of surfaces [3], interfaces, and correlated-electron materials over the last decade. However, producing VUV light required for the photoemission process in the lab has not been easy or efficient. Many experiments benefit from high flux and tunable sources.

Direct high harmonic generation (HHG) through photonic crystal fibers using ultrafast laser sources has proven to produce high intensity light for the tradeoff of slower repetition rates [1]. Scaling to faster rates has been a challenge as small focus sizes correspond to unreasonably short lengths and high gas pressures. As well, higher intensity input to produce this non-linear effect can cause damages to microstructures within such fibers. Non-linear optics has faced the challenge and using these non-linear mediums like hollow-core fibers, we are able to manipulate and generate a broadband of wavelengths. This is as within non-linear mediums; the refractive index is variable to the intensity of the laser source. This property drives multiple different processes which can create a broad band of wavelengths spanning further than 1000 nm.

Within this paper, I will be demonstrating and building an efficient source of supercontinuum light spanning into the UV using a negative curvature hollow-core optical fiber.

This stems from the motivation of the generation of short wavelengths, specifically into the UV wavelength regime. If successful, this project will lead to advanced ARPES measurements such as ultrafast time-resolved study of electron dynamics in materials.

Theory and Experimental Setup

Developing this research was segmented into two areas, autocorrelation and hollow-core fibers. Autocorrelation is a necessary concept to study ultrafast pulsed lasers. Hollow-core fibers are the backbone to driving the aspired supercontinuum, this is through multiple processes, most notably the Kerr effect.

Autocorrelation

Ultrafast laser sources in recent history have reached time scales shortening further than femtoseconds (10^{-12} sec). The Spectra Physics Tsunami® ultrafast Ti:Sapphire oscillator series will be used as the driving laser within my setup. This oscillator is pumped by the DPSS (diode pumped solid state) CW (continuous wave) green laser Spectra Physics Millennia® eV™ which is outputting at 532 nm. The mode locking mechanism of the Ti:Sapphire oscillator allows a large range of wavelengths (700 – 1000 nm) with the ability to output short femtosecond pulses (< 100 fs) and even to long picosecond pulses (< 2-100 ps) with a nominal repetition rate of 80 MHz. The ability to record the femtosecond time range, has exceeded the fastest instruments on Earth. Autocorrelation methods are used to reliably temporally characterize these ultrafast pulses for their energy, shape, duration, and spectrum [14]. This not only proves the condition of the high-repetition laser light entering the system but allows analysis of the pulse, which is necessary in any lab working with such phenomenon.

I set to construct an autocorrelation system to characterize the pulses and prove the condition of the outputting Tsunami® laser. Optical methods consist largely of interferometric type systems which is easily used to deduce the instantaneous electromagnetic field $\boldsymbol{E}(t)$.

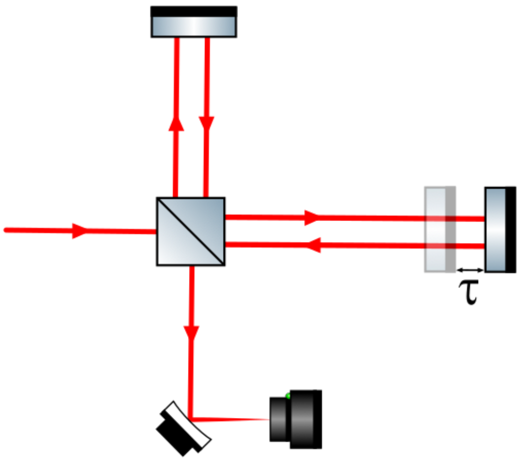

Fig. 1. Common interferometric autocorrelation setup.

The complete field is described by the sum of the two colinear pulses, which is given as a function of τ, which is the delay of the right most arm in **Fig. 1.** above:

$$\boldsymbol{E}(t,\tau) = \boldsymbol{E}(t+\tau) + \boldsymbol{E}(t). \tag{1}$$

In an ideal system, the two mirrors are at equal distance from the beam splitter. The displacement of the shaking mirror, shown on the right of **Fig. 1.** and later in **Fig. 3.**, displace by some physical distance Δx. Arriving at the time delay is simply possible by analyzing each pulse traveling at the speed of light, c (~ $3 * 10^8\ {}^{m}/_{s}$):

$$\tau = \frac{2 * \Delta x}{c}. \tag{1.1}$$

The doubling in the numerator is a result of the pulse traveling to both ends of the displacement of the mirror. Each pulse is described using the wavefunction:

$$\boldsymbol{E}(t,\tau) = A(t+\tau)e^{k(\omega(t+\tau)+\phi)} + A(t)e^{k(\omega(t+\tau)+\phi)}. \tag{1.2}$$

Where $A(t)$ is the complex amplitude and $e^{\mathrm{k}(\omega(\mathrm{t}+\tau)+\phi)}$ describes the oscillation of the wave. The characterization of the pulse alongside the evolution can be solved using Maxwell's equations. The interferometric autocorrelation trace, $I(t)$, recorded at the photodetector is the entire second harmonic electric field integrated over each individual pulse and is given as a function of τ:

$$I(\tau) \propto \int_{-\infty}^{\infty} [|\boldsymbol{E}(t+\tau) + \boldsymbol{E}(t)|^2]^2 \, dt. \tag{2}$$

Eq. (2) can now be expressed using the notation from Eq. (1.1):

$$I(\tau) \propto \int_{-\infty}^{\infty} [\left|A(t+\tau)e^{k(\omega(t+\tau)+\phi)} + A(t)e^{k(\omega(t+\tau)+\phi)}\right|^2]^2 \, dt. \tag{2.1}$$

Taking the absolute square:

$$\begin{aligned} I(\tau) \propto \int_{-\infty}^{\infty} & [A^2(t+\tau)e^{2k(\omega(t+\tau)+\phi)} + 2A(t+\tau)A(t)e^{k(\omega(t+\tau)+\phi)} \\ & + A^2(t)e^{2k(\omega(t+\tau)+\phi)}]^2 dt. \end{aligned} \tag{2.2}$$

$$\begin{aligned} \propto \int_{-\infty}^{\infty} & [|A(\mathrm{t}+\tau)|^4 + 4|A(\mathrm{t}+\tau)|^2|A(\mathrm{t})|^2 + |A(\mathrm{t})|^4 \\ & + 2A(\mathrm{t}+\tau)|A(\mathrm{t})|^2 A^*(\mathrm{t})e^{\mathrm{k}(\omega(\mathrm{t}+\tau)+\phi)} \\ & + 2A(\mathrm{t})|A(\mathrm{t}+\tau)|^2 A^*(\mathrm{t}+\tau)e^{-\mathrm{k}(\omega(\mathrm{t}+\tau)+\phi)} + A^2(t \\ & + \tau)(A^*(t))^2 e^{\mathrm{k}(\omega(\mathrm{t}+\tau)+\phi)}]dt. \end{aligned} \tag{2.3}$$

The phase, ϕ, can be taken out as both pulses are identical:

$$\begin{aligned} I(\tau) \propto \int_{-\infty}^{\infty} & [|A(t+\tau)|^4 + 4|A(t+\tau)|^2|A(t)|^2 + |A(t)|^4 \\ & + 2A(t+\tau)|A(t)|^2 A^*(t)e^{k(\omega(t+\tau))} \\ & + 2A(t)|A(t+\tau)|^2 A^*(t+\tau)e^{-k(\omega(t+\tau))} + A^2(t \\ & + \tau)(A^*(t))^2 e^{k(\omega(t+\tau))}]dt. \end{aligned} \tag{2.4}$$

This trace can be broken down into four different expressions, representing a different part of the comprised pulses. The first, is the background signal:

$$I_{back} = \int_{-\infty}^{\infty} (|A(t+\tau)|^4 + |A(t)|^4) \, dt = 2\int_{-\infty}^{\infty} (I^2(t)) \, dt. \tag{3}$$

The second, is the intensity autocorrelation function:

$$I_{intensity}(\tau) = 4\int_{-\infty}^{\infty} |A(t+\tau)|^2 |A(t)|^2 \, dt = 2\int_{-\infty}^{\infty} (I(t+\tau) \cdot I(t)) \, dt. \tag{4}$$

The third, is the coherence term associated with the angular frequency, ω:

$$I_{\omega}(\tau) = 4\int_{-\infty}^{\infty} Re\big[\big(I(t) + I(t+\tau)\big)A^*(t)A(t+\tau)e^{k(\omega(\tau))}\big] \, dt. \tag{5}$$

The fourth, is the coherence term associated with the angular frequency, 2ω:

$$I_{2\omega}(\tau) = 4\int_{-\infty}^{\infty} Re\big[A^2(t)(A^*(t+\tau))^2 e^{2k(\omega(\tau))}\big] \, dt. \tag{6}$$

Each term composes our final interferometric autocorrelation function shown in Eq. (2.4), this can be now simplified to:

$$I(\tau) = I_{back} + I_{intensity}(\tau) + I_{\omega}(\tau) + I_{2\omega}(\tau). \tag{7}$$

The function is most often normalized to the background intensity, leaving us with the final equation of the trace:

$$I_{ac}(\tau) = 1 + \frac{I_{intensity}(\tau)}{I_{back}} + \frac{I_{\omega}(\tau)}{I_{back}} + \frac{I_{2\omega}(\tau)}{I_{back}}. \tag{8}$$

The interferometric autocorrelation trace should be maximum when $\tau = 0$, as both pulses will be overlapped and constructively interfere. Solving for this maximum of Eq. (8) leaves us with:

$$I_{ac}(0) = 8. \tag{9}$$

This is from Eq. (8) which is normalized to the background intensity. Which gives us a ratio of 8:1 for the complete signal to the background. This will be used later to analyze our results.

Two-Photon Absorption. The autocorrelation trace of the setup is created from the overlap between the two pulses, separating the intensity of the trace is done through multiple different techniques which often rely on some non-linear frequency conversion. Within my own setup, I utilized the conversion process of two-photon absorption (TPA). This process takes place when two photons traveling are absorbed simultaneously and excite an atom with an increase in energy which is equal to sum of the two photon’s energies.

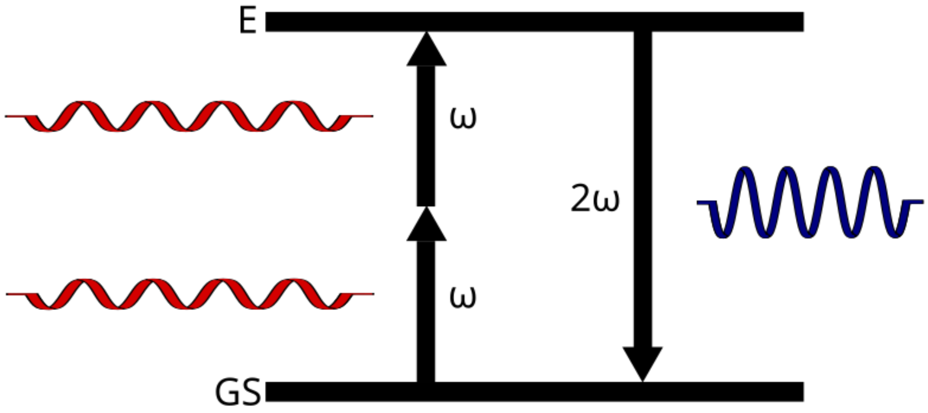

Fig. 2. Diagram representing TPA process for two photons of the same frequency, ω. As a result, this emitted photon will double in frequency, 2ω. GS stands for ground state. E stands for excited state.

Using a dielectric material or semiconductor, this process is observed if the input photon's energy is at least half of the band gap energy [15]. In the context of autocorrelation, when the two pulses overlap on this material, the frequency doubling is likely to occur. Pulses which aren't overlapped will not be absorbed and remain at their input wavelength. Using a photodiode made with a semiconductor material with a relatively low bandgap like Gallium phosphide (GaP), we could separate the Autocorrelation trace by frequency. And, if the photodiode only records higher frequencies, we could exploit this process to extract only the autocorrelation trace with minimal noise.

The output voltage, V_{out}, of the TPA process can be modeled through the equation [9]:

$$V_{out}(V) = S_{two-photon}\left(\frac{A}{W^2}\right) * G\left(\frac{V}{A}\right) * P_{input}{}^2\ (W^2) \tag{10}$$

Where $S_{two\text{-}photon}$ is the TPA coefficient, G is the transimpedance gain, and P_{input} is the input power.

First Generation Autocorrelator. The first system constructed followed the same setup shown in **Fig. 1.** and used a GaP photodiode to measure TPA processes to measure the second autocorrelation function $I_2(\tau)$. This is possible as the response of this photodiode has a wavelength range corresponding from 150 to 550 nm and at a sufficient input power. A photocurrent is developed through a photovoltaic response in the semiconductor within the detector, this is measured in the sub nano-ampere, however, is amplified with ranges of 10 dB to 70 dB, TPA should dominate over the linear absorption for the pulses outputting from 600 to 1100 nm. This fit our system ideally as the Tsunami® outputs at a variable bandwidth within this range (~700 – 1050 nm).

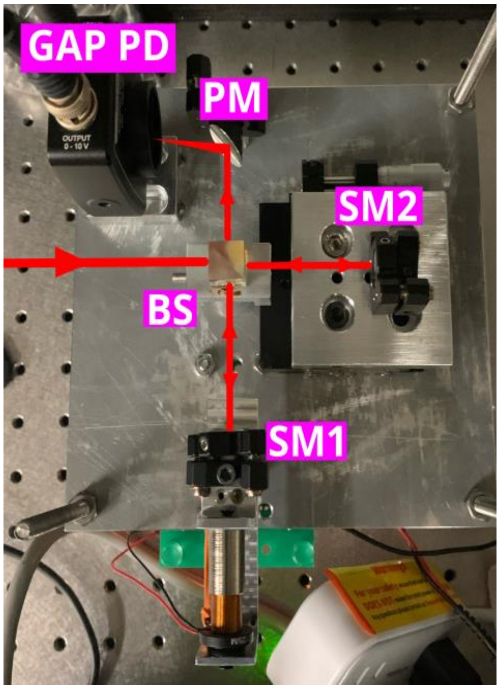

Fig. 3. First generation autocorrelation system. Interferometric setup containing a GaP photodetector. SM1 is a shaking silver mirror providing the time delay. SM2 is a still silver mirror which has a translation stage used to properly align arm lengths. BS is a 50:50 beam splitter with a low GDD provided the wavelength range. PM is an off-axis parabolic mirror with a focal length of 25 mm, meant to focus the light onto the photodetector.

The BS determines the path of the Tsunami® once entering the autocorrelation system by diverging the pulse to both SM1 and SM2 simultaneously. Once they are reflected off their respective mirror the pulses converge back in the BS and are directed to the PM (off-axis parabolic mirror) with the intention of focusing the beam onto the GaP Photodetector. Due to the overlap of multiple beams, this method is characterized as the interferometric autocorrelation trace which differs from the *intensity autocorrelation* or *background-free autocorrelation* traces [14].

The SM1 had an intention of disturbing the pulse, this was achieved by using a thin silver mirror & kinematic mount from ThorLabs (PF05-03-P01 Ø1/2" & KM05), voice coil motor (VCM), extension spring, and low-friction sliding base. The VCM was selected from the ThorLab's catalog (VC125/M) with a travel distance extending to 12.5 mm. This motor was powered from a DC power supply and driven from a DC motor driver purchased from Moticont (950 series). The driver allowed me to control the motion of the motor based on analog inputs. The analog inputs were supplied by a wave generator which let me charge an oscillating frequency to the VCM. I observed that the pushing and pulling from the system was unreliable in providing some constant oscillation which motivated the design of using an extension spring (rate of 0.157 lbs/in) from Lee Springs to pull the mirror back and use the motor to consistently drive the mirror forward. For all the data present, a constant of 6V was provided from the DC power supply and a wave spanning from frequencies of 1 to 3 Hz was selected from the wave generator. With this frequency, we could observe a displacement on the optical axis of $\Delta x = 3mm \pm 0.5\ mm$. Measurement of Δx was taken using a set of vernier calipers. This translates to a time-delay ranging between $\tau \sim 16.66\ ps - 23.33\ ps$.

The SM2 used the same mirror and mount as SM1 but was instead secured to a 0.5" single-axis translation stage with a standard micrometer from ThorLabs (MT1 with side-mounted adapter MT405). This was designed with the intention of alignment of SM2 to the equidistance middle of SM1's oscillations to extract the autocorrelation trace on the GaP Photodetector.

Confirmation that the GaP Photodetector was outputting the signal using TPA. We could use the relation between output voltage and input power represented in Eq. (4). The output voltage should be proportional to the square of the input power.

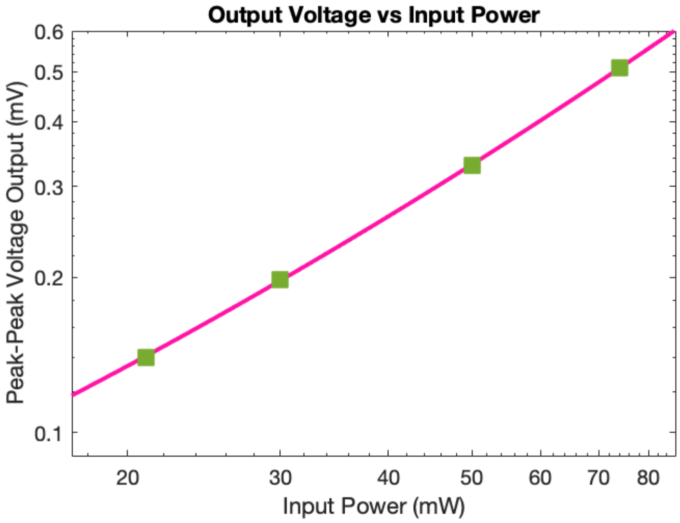

Fig. 4. Diagram showing linear trend on log plot between Peak-Peak Output Voltage (mV) vs Input Power (mW). Voltage taken using GaP Photodetector and input power recorded using power meter before Autocorrelation system.

Through **Fig. 4.**, we were unable to fit a quadratic to the output voltage over input power, suggesting that this doesn't follow the trend expected in Eq. (10). The trend observed on the log-log plot is close to ~1. This is troubling as we are not detecting the results expected from this third order non-linear effect. However, some frequency down conversion must still be happening as the detector only detects a bandwidth between 150 nm to 550 nm. This first-order detection may be a result of an insufficient detection range, as I only recorded a maximum input power of 100 mW, or a photo-voltaic response within the photodetector due to some energy conversion phenomena. The specifics of how this was possible and understanding of this process will require further research into the response.

The interferometric autocorrelation data is read out through an oscilloscope connected to the photodetector. Converting this signal of electrical intensity into to the correct time domain, we must use Eq. (2) which is the first-order autocorrelation function. This allows us to produce an interferometric trace of the pulse like the one shown in **Fig. 5.**

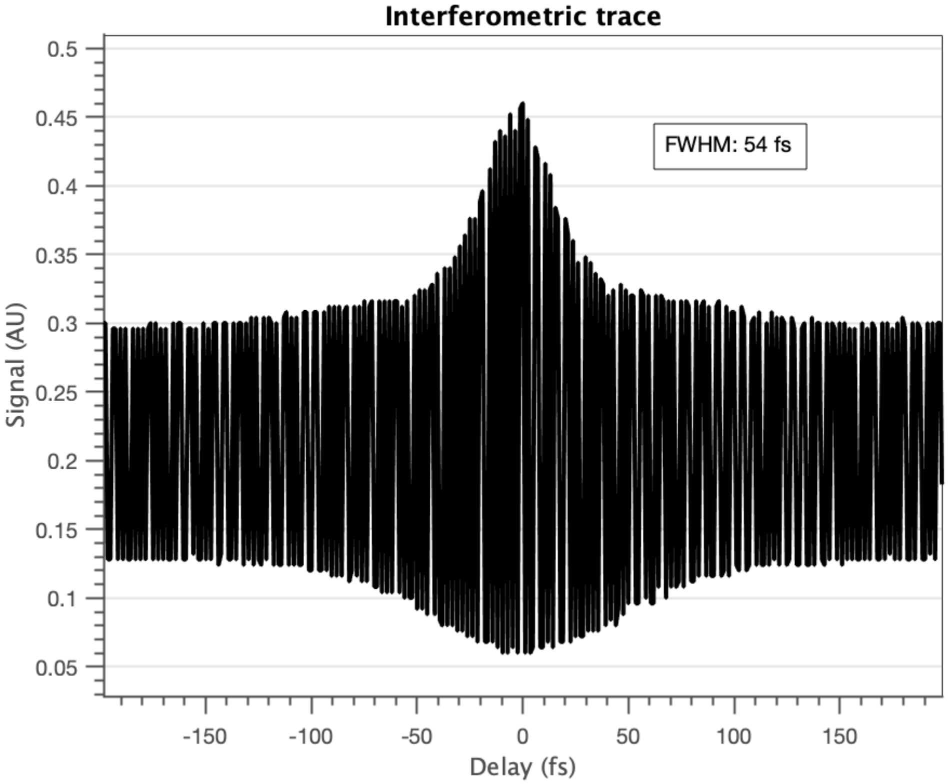

Fig. 5. Interferometric trace of Tsunami® pulse with an intensity of 71 mW entering autocorrelation system. With a FWHM representative of the pulse profile of 54 fs.

An ideal autocorrelation trace, we should detect a fringe pattern 8:1 with intensity over to under the noise. With this data, this shows approximately 4:1 and a large amount of background in-between. Changing of the alignment slightly on the autocorrelator has a large disruption to the pulse profile.

Although the background signal decreased within the scan of **Fig. 6.**, we now observe a pulse with fringe pattern far from ideal. With a ratio of approximately 14:1. The credibility of this pulse remains to be in question as the autocorrelator had faults with aligning including the shaking mirror exhibiting sporadic motion according to the same voltage. However, just the generation of such a profile allows us to confirm that our laser source is pulsing within the femtosecond pulse width regime. Future work utilizing this setup should implement a position sensor along the shaking mirror and include rails to ensure optimal distances between optics. The addition of these two will greatly increase reliability of pulse profile and allow for easier tuning of system.

Hollow-Core Fiber

A hollow-core fiber (HCF) is an optical fiber with special geometry which allows for air or gas to propagate throughout the fiber. This isn't as easy as having an optical fiber with no core as the interior as the according to the standard mechanics, the fiber core's refractive index must exceed that of its cladding surrounding the core, which is not possible with air or gas. This

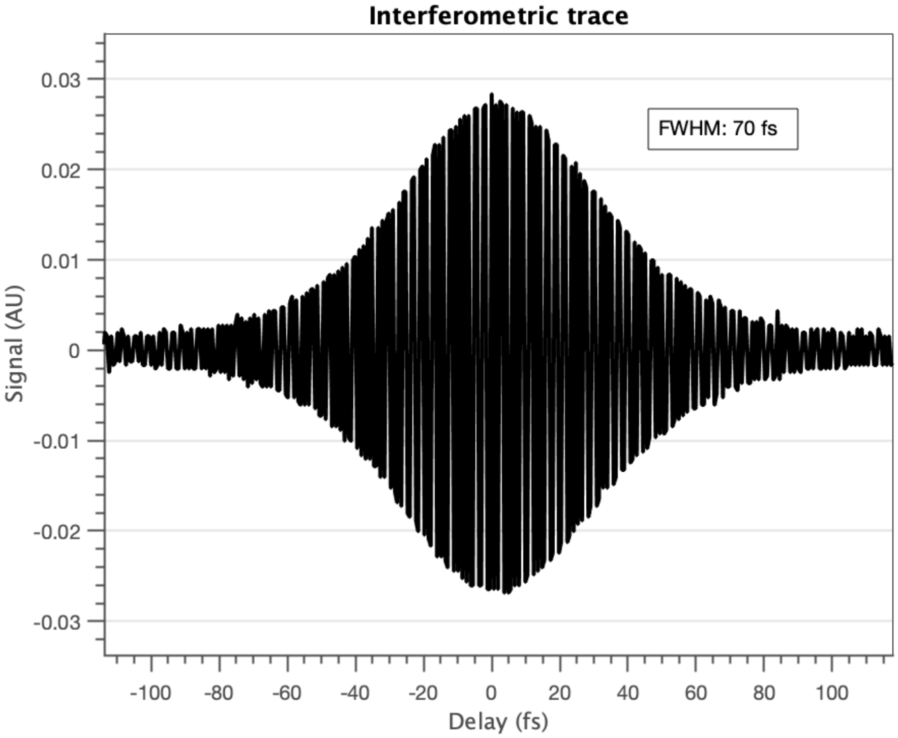

Fig. 6. Interferometric trace of Tsunami® pulse with an intensity of 50 mW entering Autocorrelation system. With a FWHM representative of the pulse profile of 70 fs.

requires a special guiding mechanism within the fiber [12]. The Hollow-Core Fiber used within our lab uses a revolver-based design shown in **Fig. 7.**

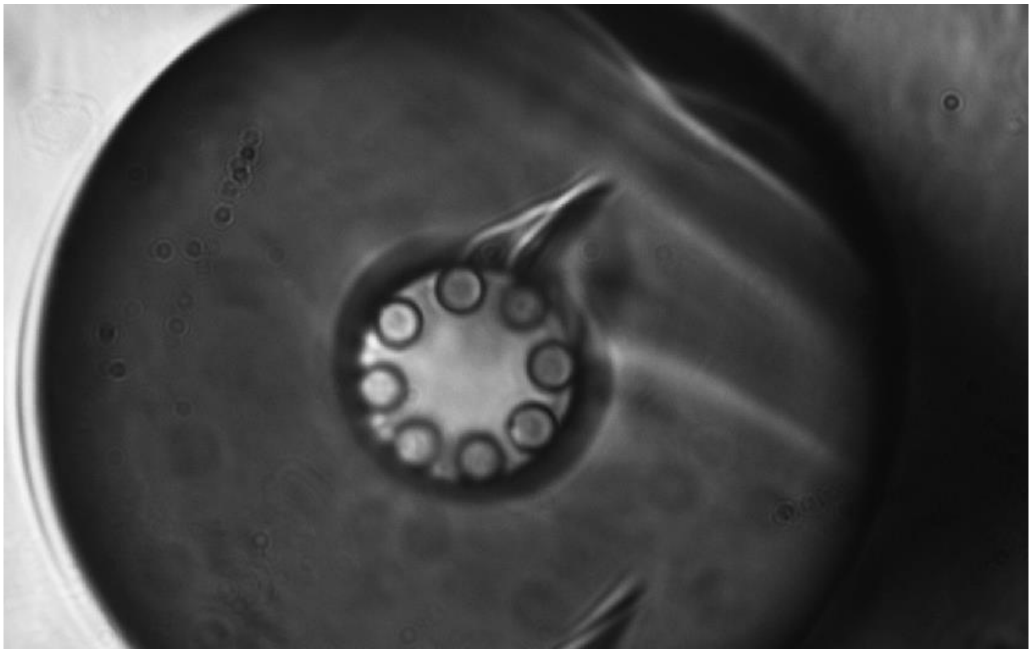

Fig. 7. Hollow-Core Fiber interior structure and capillaries taken using CCD camera installed to Olympus microscope Model BX-60.

The hollow structure through the optical axis allows for low propagation loss and the ability to insert inert gasses into the fiber. Gasses can further drive non-linear processes and is significantly important in driving HHG [12]. This is dependent on both phase matching and ionization within the medium. The pulsed laser source can output further than the fifth harmonics if these dependences are accounted for. This is useful as we can generate short wavelengths with sharp intensities.

The large bandwidth characterized by supercontinuum generation is the result of the non-linear response known as the Kerr effect [13]. The Kerr effect is directly caused due to the intensity dependence of the refractive index. This non-linear relation of refractive index is known as the Kerr nonlinearity. Three effects are drawn from Kerr nonlinearity known as cross-phase modulation (CPM), four-wave mixing (FWM), and self-phase modulation (SPM). The phase modulation of the input signal caused by this nonlinearity is known as the Kerr effect [13]. The refractive index described by the Kerr effect is:

$$n = n(\omega, |A|^2) \approx n_0(\omega) + n_{2,I}(|A|^2) \tag{11}$$

Where the refractive index, n, is dependent on the angular frequency, ω, and normalized pulse envelope, $|A|^2$. The coefficient $n_{2,I}$ is the intensity dependent refractive index. Which in the simplest models is described by:

$$n_{2,I} = n_2(I) \tag{12}$$

Both CPM and FWM have interesting impact within this field, however, my system currently doesn't have more than one set of input wavelengths/pulses. Due to this, the effect which has the most impact is SPM.

$$\frac{\partial A(x,t)}{\partial x} = -ik_0 n_{2,I}|A(x,t)|^2 A(x,t) = -j\gamma|A(x,t)|^2 A(x,t). \tag{13}$$

The term, γ is the SPM coefficient. As these pulses are collimated and propagate through the fiber by length x, the modulation within intensity causes this refractive index to modulate and therefore causes the transmitting signal's phase to modulate as well [13]. This induces spectral broadening as the modulation of the refractive index causes a frequency chirp which with the dispersion properties of HCF broadens the pulse. The chirp is proportional to the input power of the fiber.

Theoretical Setup. Theorizing propagation through this fiber could be done using simulation. For this project, I utilized the python package pyNLO [10] to generate a fiber and simulate the output frequency generation which is shown in **Fig. 8.** The python packages utilizes the non-linear Schrödinger equation to map the dispersion:

$$i\frac{\partial A(x,t)}{\partial x} = -D_2\frac{\partial^2 A}{\partial t^2} + \gamma|A(x,t)|^2 A(x,t). \tag{14}$$

The second part of the equation is derived from Eq. (13). The convention this simulation software uses to model dispersion is through the equation:

$$E_{new}(\omega) = exp(i\left(\frac{1}{2}GDD\omega^2 + \frac{1}{6}TOD\omega^3 + \frac{1}{24}FOD\omega^4\right))E(\omega). \tag{15}$$

GDD is known as Group Delay Dispersion and characterized through the dispersion coefficient β^2. While *TOD* is known as Third Order Dispersion and uses the third order dispersion coefficient β^3. And likewise, *FOD* is known as Fourth Order Dispersion, and uses the fourth order dispersion coefficient β^4. As well, this function is dependent on the frequency, ω. These values used within simulation have been assumed using the company, GLOphotonic's, data provided with the fiber [16]. Other assumptions used in the simulation are also included here within the **Table 1**:

Variable	Value
GDD: β^2	0.08742 $^{ps^2}/_{km}$
TOD: β^3	0.040 $^{ps^3}/_{km}$
FOD: β^4	0.010 $^{ps^4}/_{km}$
Pulse duration	80 fs
Pulse central wavelength	745 nm
Energy per pulse	15 nJ
Length	100 mm
Alpha	100 $\frac{dB}{km}$
Gamma	1000 $\frac{1}{W*km}$

Table 1. Containing assumptions for coefficients and constants used within simulation.

We can see that wavelengths generated (red) span over a large chunk of the spectrum, however, the pulse is completely disturbed within the temporal plane.

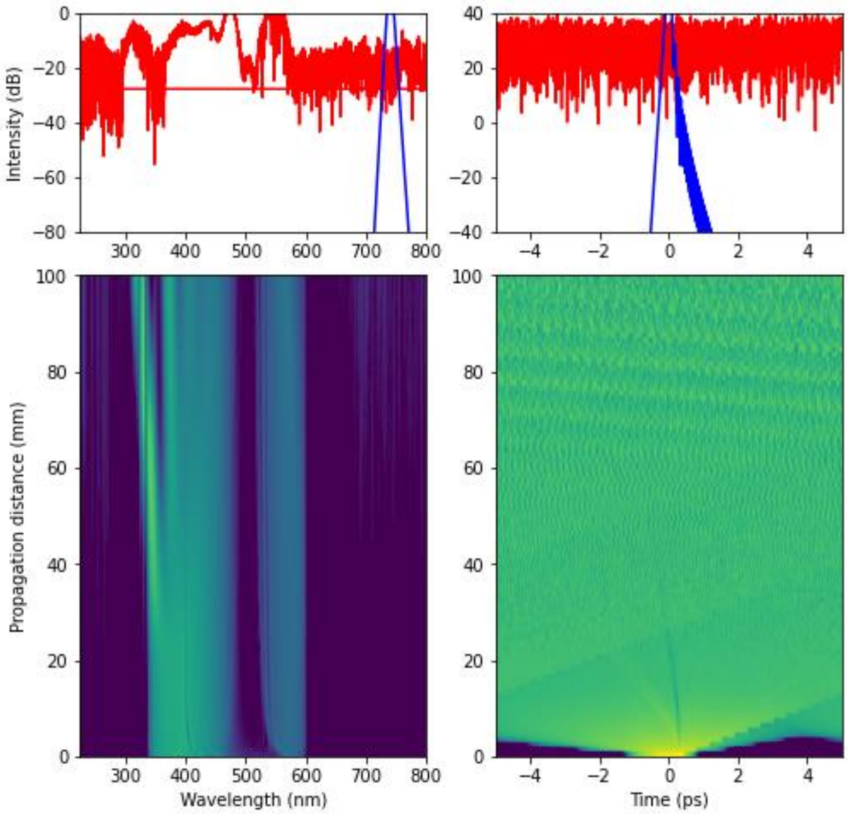

Fig. 8. Simulation of dispersed wavelengths outputting from a non-linear HCF with assumptions including a fiber length of 100 mm, pump wavelength of 745 nm, pulse width of 80 fs, pulse energy of 15 nJ, and attenuation coefficient of ~ 100 dB/km. On the right, the propagation distance and intensity of the spatial dimension of the pulses are shown. While on the left, the propagation distance and intensity of the temporal dimensions of the pulses are shown. With the top two graphs, the blue represents the input, and the red is the output.

Designing the theoretical setup required me to create some fiber enclosure which could hold the HCF up to the correct height while also allowing gas to be inserted and held within the chamber. This setup is represented below in **Fig. 9.** The laser source should enter through some lens which could focus the beam onto the entry capillaries of the fiber.

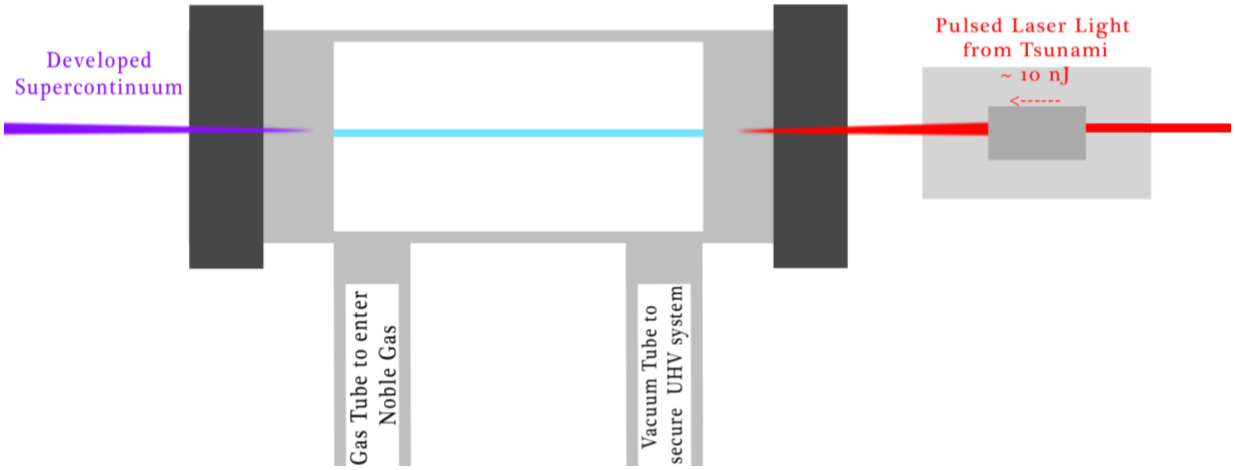

Fig. 9. Theoretical fiber-enclosure featuring entrance from the right to the exit on the left side. Starting with pulsed laser source entering through an objective lens which couples into the fiber being held in the enclosure. This source is propagated through the system and exits at the end of the fiber on the left side, with a dispersed wavelength spanning into the UV regime of the EM spectrum. Two tubes are located at the bottom of the enclosure with the motivation of making system Ultra High Vacuum (UHV) and inserting inert gases.

Experimental Setup. The experimental setup is represented within **Fig. 10.** The pulses laser source is collimated into the fiber using a 25mm objective lens held within a stationary mount attached to a translation stage on the optical axis. This stage is controlled using a micrometer. The fiber enclosure is held up to the same height and adjusted on the axis perpendicular to the optical axis using two custom mounts which individually use 3 set screws (120 degrees from each other). These allow room for optimization and transformation of the whole HCF enclosure. The output from the enclosure is directed to two bi-convex lenses which are held using a rail system. The first lens has a focal point of 100 mm and is used to collimate the beam to the focusing lens. The second, focusing, lens, has a focal point of 35 mm and focuses the beam into the slit of the spectrometer. Each viewport and lens use fused silica as opposed to traditional glass as transmission below 300 nm is blocked with glass.

During my research, I was unable to include aspects of UHV as the necessary parts exceeded my budget. However, I was able to direct gas through one tube and leave the other open, simulating 1 atm pressure of inert gas within the enclosure.

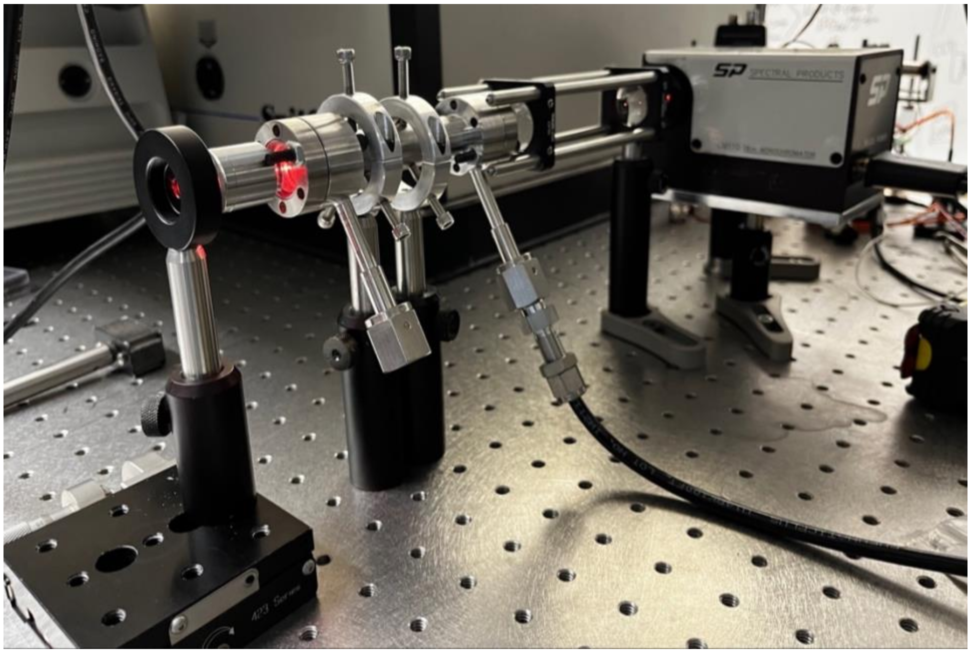

Fig. 10. Experimental fiber-enclosure with entrance on the left side and exiting toward spectrometer on the right. On the left, before the fiber enclosure is the objective lens. This focuses the light into the fiber enclosure which is held on two posts in the middle. The output is this collimated and focused into the spectrometer using two lenses. The spectrometer (CM110) is shown on the right upper corner of the image.

Data. Collection of data was done using the spectrometer, CM110. This spectrometer uses mirrors and a grating to direct specific wavelengths to its output slit which is then read by a photodiode. This allowed me to take scans over a range of wavelengths and plot the intensity of that wavelength outputting from the system. The photodiode used within my setup has a reliable range spanning from 190 to 1000 nm. Shown in **Fig. 11.** and **Fig. 12.** are a scans comparing wavelengths recorded out of the HCF vs no HCF. The voltage directed to the PD was the same in both instances, with a HCF and without. This was done to account for possible noise recorded by the photodiode and prove that wavelengths aside from the pump were being generated.

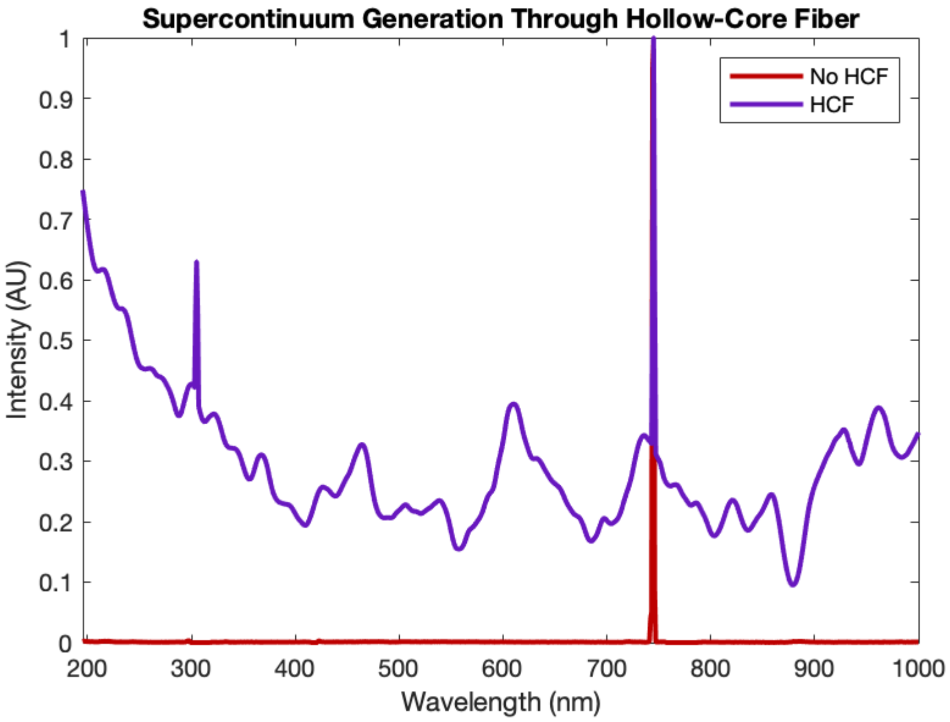

Fig. 11. Spectra recorded with spectrometer, spanning 190 nm to 1000 nm. Two data sets taken, one with HCF (purple) and the other with no HCF (red). This data was taken with pump wavelength centering 745 nm. October 27, 2022.

Discussion. Between **Fig. 11.** and **Fig. 12.** the input angles were changed significantly. The two different trends represented in each data set suggest that different effects are dominating due to the geometry. **Fig. 11.** shows a large bandwidth stretching over the entire regime with one significant peak other than the pump wavelength. This super-continuum seems to be the result of the Kerr effect. While **Fig. 12.** shows peaks in intensity over specific wavelengths between 250 to 300 nm, 350 to 400 nm, and 425 to 475 nm. These peaks suggest that some harmonic generation might be at play.

The exact wavelengths of the output within **Fig. 12.** have a significantly larger error margin, estimated to be off by ±50 nm. This offset was due to a non-perfect optimization of the grating within the CM110 spectrometer. This might be the reason why the peaks don't directly correlate in wavelength to the harmonics of the pump wavelength (2nd at 370 nm and 3rd at 185 nm). The peak within this figure, between 250 to 300 nm seems to be aptly reflected within **Fig. 11.**, however, none of the others are represented. This is specifically questionable surrounding the largest peak in **Fig. 12.** (between 425 to 475 nm). The generation of these wavelengths may not have occurred due to a change of inclination of the fiber on the optical axis. Generation of intensities spanning into the sub 200 nm range increases in both trials which is promising regarding our motivation of generation into this wavelength range.

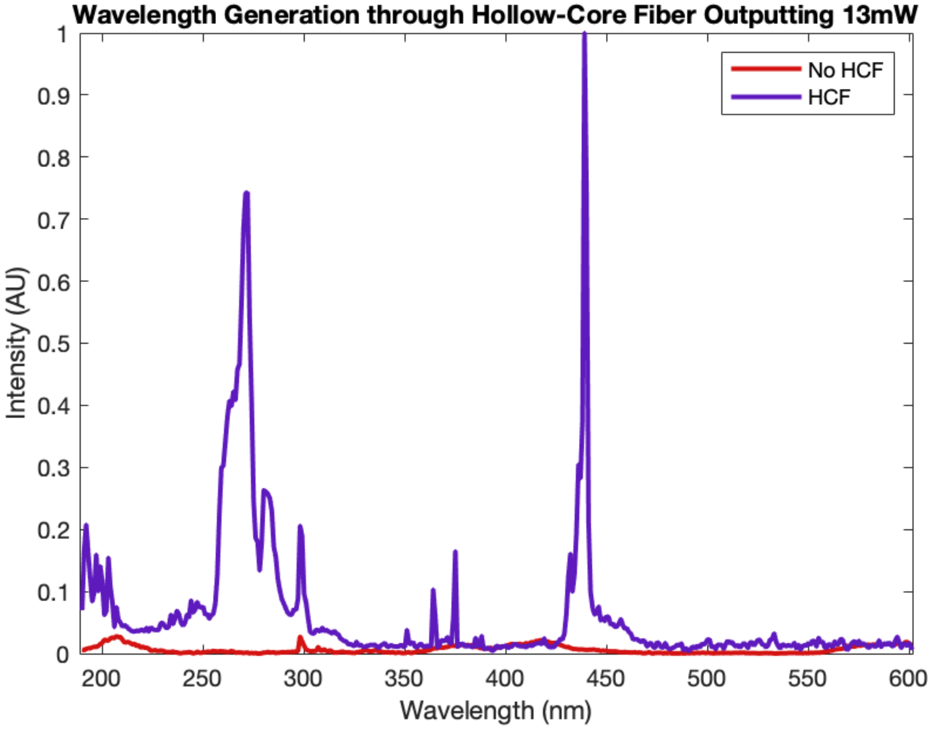

Fig. 12. Spectra recorded with spectrometer, spanning 190 nm to 605 nm. Two data sets taken, one with HCF (purple) and the other with no HCF (red). This data was taken with pump wavelength centering 740 nm. September 16, 2022.

The broad band generation which is shown in **Fig. 1.** is reflective of the simulated data from **Fig. 8.** But also peaks roughly between 300 to 350 nm and 450 to 500 nm which might correlate to the two largest peaks within **Fig. 12.** Confirmation of this will not be possible without further data collection with comprehensive data representing the angular dependency of input angle.

Summary and Future Works

During my research at the University of Arkansas, in my undergraduate studies, I was able to develop a supercontinuum spanning into the UV region of the electromagnetic spectrum using a mode-locked laser with a pump wavelength of 745 nm. This conclusion followed small feats which notably included aligning/lasing Tsunami® laser, designing/creating Autocorrelation system, and designing/experimenting with HCF. The generation of broad wavelengths into the deep UV may be exploited within electro spectroscopy systems including ARPES and potentially into silicon wafer patterning. Further research should expand on securing system and researching dependencies within it including but not limited to gas implementation, UHV + pressure control, energy dependence, and angle dependence. With this understanding, replicating such results will be increasingly easier. Alongside, the creation of a collinear and non-collinear interferometric autocorrelation system will further research into pulse measurement and profile before and after fiber system.

References

1. David E. Couch, Daniel D. Hickstein, David G. Winters, Sterling J. Backus, Matthew S. Kirchner, Scott R. Domingue, Jessica J. Ramirez, Charles G. Durfee, Margaret M. Murnane, and Henry C. Kapteyn, "Ultrafast 1 MHz vacuum-ultraviolet source via highly cascaded harmonic generation in negative-curvature hollow-core fibers," Optica 7, 832-837 (2020)

2. Eich, S., et al. "Time- and Angle-Resolved Photoemission Spectroscopy with Optimized High-Harmonic Pulses Using Frequency-Doubled Ti:Sapphire Lasers." *Journal of Electron Spectroscopy and Related Phenomena*, vol. 195, 2014, pp. 231–236., doi:10.1016/j.elspec.2014.04.013.

3. "Electrical Measurements of Surfaces and Interfaces." *An Essential Guide to Electronic Material Surfaces and Interfaces*, 2016, pp. 22–41., doi:10.1002/9781119027140.ch3.

4. Jaurigue, L. (2017). Mode-Locked Laser Model. *Springer Theses Passively Mode-Locked Semiconductor Lasers,* 15-31. doi:10.1007/978-3-319-58874-2_2

5. L'Huillier, A. (2017). Multiple harmonic conversion of 1064 nm in rare gases. *Journal of Physics B: Atomic, Molecular and Optical Physics, 50*(6), 060501. doi:10.1088/1361-6455/aa5935

6. Paschotta, Rüdiger. "Pulse Duration and Pulse Energy." *Field Guide to Laser Pulse Generation*, doi:10.1117/3.800629.p20.

7. *Advances in Imaging and Electron Physics*, 2013, p. iii., doi:10.1016/b978-0-12-407755-3.21001-7.

8. "Synchrotron Radiation: Properties." *The Physics of Synchrotron Radiation*, 2004, pp. 81–114., doi:10.1017/cbo9780511534973.007.

9. Shin, Seong-Il, and Yong-Sik Lim. "Simple Autocorrelation Measurement by Using a GaP Photoconductive Detector." *Journal of the Optical Society of Korea*, vol. 20, no. 3, 2016, pp. 435–440., doi:10.3807/josk.2016.20.3.435.

10. G. Ycas, D. Maser, and D. D. Hickstein, PyNLO—Python Package for Nonlinear Optics (GitHub Repository, 2018), https://github.com/PyNLO/PyNLO.

11. Yu, Fei, and Jonathan C. Knight. "Negative Curvature Hollow-Core Optical Fiber." *IEEE Journal of Selected Topics in Quantum Electronics*, vol. 22, no. 2, 2016, pp. 146–155., doi:10.1109/jstqe.2015.2473140.

12. Paschotta, Dr. Rüdiger. "Hollow-Core Fibers." *Hollow-Core Fibers, Explained by RP Photonics Encyclopedia; Photonic Bandgap Fibers, Air-Guiding Fibers*, RP Photonics AG, 11 Oct. 2022, www.rp-photonics.com/hollow_core_fibers.html.

13. Paschotta, Dr. Rüdiger. “Kerr Effect.” *Kerr Effect, Explained by RP Photonics Encyclopedia; DC Kerr Effect, Kerr Cells, AC Kerr Effect, Nonlinearity, Self-Phase Modulation, Fiber, Nonlinear Polarization, Self-Steepening*, RP Photonics AG, 23 Sept. 2022, www.rp-photonics.com/kerr_effect.html.

14. Trebino, Rick. “Interferometric Autocorrelation.” *Interferometric Autocorrelation, Tutorial by Swamp Optics; Tutorial, Autocorrelation, Interferometric Autocorrelation*, Swamp Optics, 2015, www.swampoptics.com/assets/tutorials_interferometric_autocorrelation.pdf.

15. Rumi, Mariacristina, and Joseph W. Perry. “Two-Photon Absorption: An Overview of Measurements and Principles.” *Advances in Optics and Photonics*, vol. 2, no. 4, 2010, p. 451., https://doi.org/10.1364/aop.2.000451.

16. “Hollow-Core Photonic Crystal Fibers.” *Glophotonics*, www.glophotonics.fr/index.php/hollow-core-photonic-crystal-fibers.html.